Trade-off Between Probability of Detection and Achievable Rate in Near-Field ISAC Systems

Mayushi Amaya Jayasinghe, Janith Kavindu Dassanayake, and Gayan Amarasuriya
School of Electrical, Computer, and Biomedical Engineering, Southern Illinois University, Carbondale, IL, USA 62901
Email: {mayushi.jayasinghe,janith.dassanayake,gayan.baduge}@siu.edu

***Abstract*—The transition to millimeter-wave and sub-THz frequency bands necessitates that the base-stations (BSs) utilize extra-large antenna arrays (ELAA) to compensate for the associated huge path-losses. However, when higher frequencies and shorter transmission distances are utilized, the spherical wave curvature can no longer be neglected. Hence, the ELAA-based wireless systems tend to operate primarily in the near-field. Thus, the far-field channel models used for near-field users may detrimentally affect wireless system designs and performance gains. To this end, we investigate the impact of mismatches between far-field and near-field channel models/precoders on the performance of ELAA-based integrated sensing and communication (ISAC). To this end, the achievable user rates are derived for the near-field. Two detectors for sensing a target are designed based on known/unknown BS/target channels. The performance of these detectors are investigated by deriving the probability of detection and probability of false-alarm. A transmit power optimization procedure is also proposed to maximize the minimum achievable user rate, while ensuring a power threshold for sensing. Numerical results are used to study the fundamental trade-off between the probability of detection and achievable rates for near-field ELAA-based ISAC. We unveil that ELAAs can be leveraged to improve the ISAC performance trade-offs.**

I. Introduction

The communication and sensing tasks are used to be carried out in separate spectrum allocations using dedicated hardware platforms. Since the communication spectrum tends to merge with sensing frequencies, integrated sensing and communication (ISAC) has been envisioned for the next-generation wireless systems [1]–[3]. In ISAC, communication and sensing tasks share the available spectrum and hardware resources, enabling a unified architecture for both functionalities [4]. As a result of this integrated design, both the communication and sensing performance can be boosted, while improving the spectrum utilization and reducing the hardware/implementation cost [1], [4]. Thus, ISAC has recently attracted tremendous research interests in a myriad of directions [5]–[8].

In [5], a joint transmit and receive beamformer design for ISAC systems has been developed to maximize the signal-to-interference-plus-noise ratio (SINR) at the receiver. In [6], a non-orthogonal multiple access-aided ISAC framework has been studied by superimposing communication with sensing signals. In [6], a beamformer design problem is formulated to optimize the communication rate and received signal power for sensing. In [7], a full-duplex ISAC system has been proposed to transmit communication signals during the waiting time interval of conventional pulsed radars. In [7], an ISAC system has been proposed to increase the achievable rate while mitigating near-target blind range issue, and its performance has been compared against the radar-centric pulsed waveform embedded with communication signals. In [8], the probability of false-alarm and detection have been derived, and the performance trade-off has been studied for a far-field ISAC system. In [9], the energy efficiency of a multi user ISAC system is maximized, while ensuring sensing requirements in terms of individual radar beam pattern gains, via successive convex approximation and semi-definite relaxation techniques.

The ISAC systems are anticipated to function in recently acquired mid-band (7-15 GHz), millimeter-wave, and sub-THz frequency bands. Consequently, it signifies the necessity of deploying extra-large antenna arrays (ELAAs) at the base-stations (BSs) to compensate for the path-losses resulting due to higher frequencies [1]. The transition from the compact antenna arrays to ELAAs not only results in large array apertures but also fundamentally alters electromagnetic (EM) propagation characteristics [10]. The EM radiation field of an antenna array can be divided into three regions, namely the reactive near-field, the radiative near-field, and the far-field [10]. In typical wireless systems, the far-field propagation is assumed in which the channels are modeled through planar wavefronts. Whereas in the radiative near-field, the channels should be modeled via spherical-waves [10]. The boundary which separates near-field and far-field is quantified by Fraunhofer/Rayleigh distance, which is directly proportional to the square of the array's aperture and inversely proportional to the wavelength. In the current state-of-the-art, the BSs use compact antenna array, and hence, the near-field propagation is insignificant. However, the radiative near-field is more likely to be extended up to hundreds of meters when ELAAs operating in millimeter-wave and sub-THz frequencies are deployed. Hence, the users/targets served by these ELAAs are more likely to be located within the near-field. In [10], a novel channel model has been proposed to accurately model the near-field line-of-sight (LoS) channels. By adopting this near-field LoS channel model, [11] unveils that the classical far-field channel model may become inaccurate for the ELAAs operating at millimeter-waves.

Despite the aforementioned research efforts on ISAC [5]–[8] with far-field channel models, the characterization of fundamental performance trade-offs in the near-field channel model in [10] is also a necessity for ELAAs. Having being inspired, we investigate the trade-off between the achievable rate and probability of detection for ELAA-aided near-field ISAC systems. By adopting computationally-efficient maximal ratio transmission (MRT)-based precoders, the achievable user rates are quantified. Two detectors based on Neyman-Pearson (NP) lemma and the generalized likelihood ratio test (GLRT) criterion are derived for target detection with/without

ICC 2025 - IEEE International Conference on Communications | 979-8-3315-0521-9/25/$31.00 ©2025 IEEE | DOI: 10.1109/ICC52391.2025.11161613

$$\xi_{mk} = \frac{1}{12\pi}\sum_{i=0}^{1}\sum_{j=0}^{1}\frac{\alpha_i(x_{mk})\alpha_j(y_{mk})\,|z_k|}{\left(\alpha_j^2(y_{mk})+z_k^2\right)\sqrt{\alpha_i^2(x_{mk})+\alpha_j^2(y_{mk})+z_k^2}} + \frac{1}{6\pi}\sum_{i=0}^{1}\sum_{j=0}^{1}\tan^{-1}\left(\frac{\alpha_i(x_{mk})\alpha_j(y_{mk})}{|z_k|\sqrt{\alpha_i^2(x_{mk})+\alpha_j^2(y_{mk})+z_k^2}}\right). \quad (2)$$

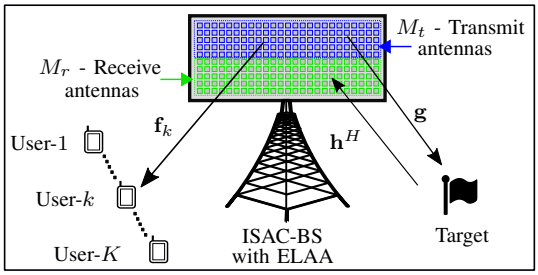

Fig. 1. An ELAA-based ISAC system.

sensing channel knowledge. The performance of two detectors is evaluated via the receiver operating characteristics (ROC). A transmit power optimization procedure is also proposed to maximize the minimum achievable user rate, while satisfying a predefined threshold sensing power. The rate-detection trade-off is optimized via transmit power allocation. Our results unveil that the mismatches between precoders designed based on far/near-field channel assumptions degrade the ISAC performance gains. Thus, we advocate to classify the users/targets based on Fraunhofer distance and use the relevant near/far-field precoders in designing ELAA-based ISAC systems.

II. System, Channel and Signal Models

A. System model

We consider an ISAC system in which an ELAA-based BS communicates with K single-antenna users while sensing a target (see Fig. 1). The ELAA has M_t/M_r transmit/receive antennas, which are arranged as a uniform rectangular planar array (URPA) with M_h rows and M_v columns. We consider that the URPA is centered around the origin of the XY-plane. Each antenna element has an area of A. Antennas are spaced at d_h and d_v along the horizontal and vertical directions, respectively. This leads to an array with a width and a height of $L_h = M_h\sqrt{A}+(M_h-1)d_h$ and $L_v = M_v\sqrt{A}+(M_v-1)d_v$, respectively. The antennas are indexed from left to right, starting from the bottom row to the top row. The coordinates of the mth antenna can be written as $\mathbf{p}_m = [x_m, y_m, 0]^T$, where $x_m = \Delta_h\big[-(M_h-1)/2 + \mathrm{mod}(m-1, M_h)\big]$ and $y_m = \Delta_v(-(M_v-1)/2 + \lfloor(m-1)/M_h\rfloor)$. Here, we define $\Delta_h = \sqrt{A}+d_h$ and $\Delta_v = \sqrt{A}+d_v$. The Fraunhofer distance of the ELAA is given by $d_F = 2(L_h^2+L_v^2)/\lambda$ [12, Eq. (3)].

B. Channel model

We assume that the users and target are located within the near-field of ELAA such that the transmission distances are below d_F. Hence, both communication and sensing channels need to be modeled by using the spherical wavefront-based near-field model. The location of the kth user is defined as $\mathbf{u}_k = [x_k, y_k, z_k]^T$. hence, the azimuth and elevation angles at the ELAA can be defined as $\omega_k = \tan^{-1}(x_k/z_k)$ and $\varphi_k = \tan^{-1}(y_k/\sqrt{x_k^2+z_k^2})$, respectively.

We define the channel vector between the BS and the kth user as $\mathbf{f}_k = [f_{1k}, \cdots, f_{M_t k}] \in \mathbb{C}^{1\times M_t}$. Here, $f_{mk} = |f_{mk}|\,e^{-j\delta_{mk}}$ is the channel between the mth antenna of the ELAA and the kth user. The channel amplitude and phase are denote by $|f_{mk}|$ and $\delta_{mk} \in [0, 2\pi)$, respectively. They can be modeled as [11]

$$|f_{mk}| = \sqrt{\xi_{mk}} \quad \text{and} \quad \delta_{mk} = 2\pi \bmod (||\boldsymbol{\kappa}_{mk}||/\lambda, 1), \quad (1)$$

where ξ_{mk} is the free-space channel gain at the mth antenna located at $\mathbf{p}_m$, and it is defined as (2) at the top of this page. In (2), $\alpha_i(\beta) \triangleq \sqrt{A}/2+(-1)^i\beta$, $x_{mk} = x_m - x_k$, and $y_{mk} = y_m - y_k$ [11]. In (1), $\boldsymbol{\kappa}_{mk} = \mathbf{p}_m - \mathbf{u}_k$, and λ is the wavelength. The direct and reflected channels of the target are denoted by $\mathbf{g} \in \mathbb{C}^{1\times M_t}$ and $\mathbf{h}^H \in \mathbb{C}^{M_r\times 1}$, respectively. These sensing channels can also be modeled similarly to $\mathbf{f}_k$.

C. ISAC signal model

A sensing signal is transmitted along with the information-bearing communication signals. The signal transmitted by the BS can be written as

$$\mathbf{s} = \sqrt{\rho_s P}\mathbf{w}_s s_s + \sum\nolimits_{k=1}^{K}\sqrt{\rho_{c,k}P}\mathbf{w}_{c,k}s_{c,k}, \quad (3)$$

where $\mathbf{s} \in \mathbb{C}^{M_T\times 1}$, ρ_s is the transmit power allocation coefficient for the sensing signal, P is the total transmit power available at the BS, $\mathbf{w}_s$ is the sensing precoder, s_s is the sensing signal satisfying $\mathbb{E}[|s_s|^2] = 1$, $\rho_{c,k}$ is the transmit power allocation coefficient for the the kth communication user, $\mathbf{w}_{c,k}$ is the kth user's precoder, and $s_{c,k}$ is the communication signal intended for the kth user. The normalized sensing and communication precoders can be designed via MRT principle to minimize the computational complexity as

$$\mathbf{w}_s = \mathbf{g}^H/\sqrt{\mathrm{Tr}(\mathbf{g}^H\mathbf{g})} \quad \text{and} \quad \mathbf{w}_{c,k} = \mathbf{f}_k^H/\sqrt{\mathrm{Tr}(\mathbf{f}_k^H\mathbf{f}_k)}, \quad (4)$$

where $\mathbf{g}$ is the BS-target sensing channel, and $\mathbf{f}_k$ is the BS-kth communication channel. The signal received at the kth user can be written as

$$y_k = \mathbf{f}_k\mathbf{s} + n_k = \sqrt{\rho_s P}\mathbf{f}_k\mathbf{w}_s s_s + \sqrt{\rho_{c,k}P}\mathbf{f}_k\mathbf{w}_{c,k}s_{c,k} + \sum\nolimits_{i\neq k}^{K}\sqrt{\rho_{c,i}P}\mathbf{f}_k\mathbf{w}_{c,i}s_{c,i} + n_k, \quad (5)$$

where the first term in (5) is the sensing signal interference, and the second term is the desired signal of the kth user. The third term is the inter-user interference, and $n_k \sim \mathcal{CN}(0, \sigma_k^2)$ is an additive white Gaussian noise (AWGN) at the kth user.

The received SINR at the kth user can be written as

$$\gamma_k = \frac{\rho_{c,k}P|\mathbf{f}_k\mathbf{w}_{c,k}|^2}{\rho_s P|\mathbf{f}_k\mathbf{w}_s|^2 + P\sum_{i\neq k}^{K}\rho_{c,i}|\mathbf{f}_k\mathbf{w}_{c,i}|^2 + \sigma_k^2}. \quad (6)$$

From (6), an achievable DL user rate at the kth communication user can be written as

$$\mathcal{R}_k = \log_2(1+\gamma_k). \quad (7)$$

III. Sensing Model

The detection hypotheses are formulated based on the presence/absence of the target. Thus, the null hypothesis ($\mathcal{H}_0$) defines a case in which the target is absent in the sensing environment. The alternate hypothesis ($\mathcal{H}_1$) represents the case in which the target is present.

A. Formulation of the target detectors

The null hypothesis can be written as

$$\mathcal{H}_0 : \mathbf{y} = \mathbf{Z}\mathbf{s} + \mathbf{n}, \tag{8}$$

where $\mathbf{Z} \in \mathbb{C}^{M_r \times M_t}$ is the self-interference matrix, and $\mathbf{n} \sim \mathcal{CN}(\mathbf{0}, \sigma^2\mathbf{I})$. By employing successive interference cancellation for ISAC, the self-interference power can be mitigated [13]. The (p,q)th element of the self-interference matrix $\mathbf{Z} \in \mathbb{C}^{M_r \times M_t}$ can be modeled as [14], [15]

$$[\mathbf{Z}]_{p,q} = \sqrt{\delta_{p,q}} e^{-j2\pi \frac{\Delta_{p,q}}{\lambda}}, \tag{9}$$

where $\delta_{p,q} > 0$ and $\Delta_{p,q} > 0$ denote the residual self-interference channel power and the distance between the qth transmit antenna and the pth receive antenna, respectively.

The alternate hypothesis can be written as

$$\mathcal{H}_1 : \mathbf{y} = \mathbf{h}^H\mathbf{g}\mathbf{s} + \mathbf{Z}\mathbf{s} + \mathbf{n} = \mathbf{H}\mathbf{s} + \mathbf{Z}\mathbf{s} + \mathbf{n}, \tag{10}$$

where $\mathbf{g} \in \mathbb{C}^{1\times M_t}$ and $\mathbf{h}^H \in \mathbb{C}^{M_r \times 1}$ are the DL and UL channels between the BS and target, respectively, and we denote $\mathbf{H} = \mathbf{h}^H\mathbf{g}$ as the composite BS-target channel.

1) Case-1 (Known channel $\mathbf{H}$): We assume $\mathbf{Z}$, $\mathbf{s}$, $\mathbf{H}$ and the covariance matrix of AWGN are known. The distributions of the signals in (8) and (10) can be written as

$$\mathcal{H}_0 : \mathbf{y} \sim \mathcal{CN}(\mathbf{m}_0, \sigma^2\mathbf{I}), \tag{11a}$$

$$\mathcal{H}_1 : \mathbf{y} \sim \mathcal{CN}(\mathbf{m}_1, \sigma^2\mathbf{I}), \tag{11b}$$

where $\mathbf{m}_0 = \mathbf{Z}\mathbf{s}$ and $\mathbf{m}_1 = \mathbf{H}\mathbf{s}+\mathbf{Z}\mathbf{s}$. The NP detector decides $\mathcal{H}_1$ if [16]

$$\mathcal{L}(\mathbf{y}) = \frac{f(\mathbf{y};\mathcal{H}_1)}{f(\mathbf{y};\mathcal{H}_0)} > \kappa, \tag{12}$$

where $\mathcal{L}(\mathbf{y})$ is the likelihood ratio and κ is a detection threshold. In (12), $f(\mathbf{y};\mathcal{H}_0)$ and $f(\mathbf{y};\mathcal{H}_1)$ are the probability density functions (PDFs) of $\mathbf{y}$ under $\mathcal{H}_0$ and $\mathcal{H}_1$, respectively. By using (11a) and (11b), the PDFs in (12) can be written as

$$f(\mathbf{y};\mathcal{H}_0) = \frac{e^{-(\mathbf{y}-\mathbf{m}_0)^H \frac{1}{\sigma^2}\mathbf{I}^{-1}(\mathbf{y}-\mathbf{m}_0)}}{\pi^{M_r}\det(\sigma^2\mathbf{I})}, \tag{13a}$$

$$f(\mathbf{y};\mathcal{H}_1) = \frac{e^{-(\mathbf{y}-\mathbf{m}_1)^H \frac{1}{\sigma^2}\mathbf{I}^{-1}(\mathbf{y}-\mathbf{m}_1)}}{\pi^{M_r}\det(\sigma^2\mathbf{I})}. \tag{13b}$$

Next, the likelihood ratio in (12) can be rewritten as

$$\mathcal{L}(\mathbf{y}) = \frac{e^{-(\mathbf{y}-\mathbf{m}_1)^H \frac{1}{\sigma^2}\mathbf{I}^{-1}(\mathbf{y}-\mathbf{m}_1)}}{e^{-(\mathbf{y}-\mathbf{m}_0)^H \frac{1}{\sigma^2}\mathbf{I}^{-1}(\mathbf{y}-\mathbf{m}_0)}} > \kappa. \tag{14}$$

The log-likelihood ratio can be obtained by taking the logarithm of (14). Thus, the NP detector decides $\mathcal{H}_1$ if

$$\mathcal{T}(\mathbf{y}) = \mathbf{y}^H(\mathbf{m}_1 - \mathbf{m}_0) = \mathbf{y}^H\mathbf{H}\mathbf{s} > \kappa', \tag{15}$$

where the modified threshold κ' is given by

$$\kappa' = (1/2)\sigma^2\ln(\kappa) + (1/2)\mathbf{s}^H\mathbf{H}^H\mathbf{H}\mathbf{s} + \mathbf{s}^H\mathbf{Z}^H\mathbf{H}\mathbf{s}. \tag{16}$$

In (15), $\mathcal{T}(\mathbf{y})$ is a sufficient test statistic for the NP detector. The PDFs of the test statistic $\mathcal{T}(\mathbf{y})$ under $\mathcal{H}_0$ and $\mathcal{H}_1$ can be written as

$$\mathcal{H}_0 : \mathcal{T}(\mathbf{y}) \sim \mathcal{CN}(\tilde{m}_0, \tilde{v}_0), \tag{17a}$$

$$\mathcal{H}_1 : \mathcal{T}(\mathbf{y}) \sim \mathcal{CN}(\tilde{m}_1, \tilde{v}_1), \tag{17b}$$

where $\tilde{m}_0$, $\tilde{m}_1$, $\tilde{v}_0$ and $\tilde{v}_1$ can be derived as (Appendix A)

$$\tilde{m}_0 = \mathbf{s}^H\mathbf{Z}^H\mathbf{H}\mathbf{s} \quad \text{and } \tilde{m}_1 = \mathbf{s}^H\mathbf{H}^H\mathbf{H}\mathbf{s} + \mathbf{s}^H\mathbf{Z}^H\mathbf{H}\mathbf{s}, \tag{18}$$

$$\tilde{v}_0 = \sigma^2\mathbf{s}^H\mathbf{H}^H\mathbf{H}\mathbf{s}, \quad \text{and } \tilde{v}_1 = \sigma^2\mathbf{s}^H\mathbf{H}^H\mathbf{H}\mathbf{s}. \tag{19}$$

Next, the probability of false alarm (P_{FA}) can be defined as

$$P_{FA} = \Pr\left(\mathcal{T}(\mathbf{y}) > \kappa';\mathcal{H}_0\right), \tag{20}$$

where κ' is given in (16). By using the complementary cumulative distribution function (CCDF) of the Gaussian distribution [16], P_{FA} can be derived as

$$P_{FA} = \mathcal{Q}\left((\kappa' - \tilde{m}_0)/\sqrt{\tilde{v}_0}\right), \tag{21}$$

where $\mathcal{Q}(\cdot)$ is the Gaussian Q-function. Moreover, for a fixed P_{FA}, the modified threshold κ' can be computed as

$$\kappa' = \sqrt{\tilde{v}_0}\mathcal{Q}^{-1}(P_{FA}) + \tilde{m}_0. \tag{22}$$

The probability of detection (P_D) can be derived via (22) as

$$P_D = \Pr\left(\mathcal{T}(\mathbf{y}) > \kappa';\mathcal{H}_1\right) = \mathcal{Q}\left((\kappa' - \tilde{m}_1)\Big/\sqrt{\tilde{v}_1}\right). \tag{23}$$

2) Case-2 (Unknown channel $\mathbf{H}$): We assume $\mathbf{Z}$, $\mathbf{s}$ and the covariance matrix of AWGN are known, but $\mathbf{H}$ is unknown. The distributions of the signals in (8) and (10) are written as

$$\mathcal{H}_0 : \mathbf{y} \sim \mathcal{CN}(\mathbf{m}_0^\dagger, \sigma^2\mathbf{I}), \tag{24a}$$

$$\mathcal{H}_1 : \mathbf{y} \sim \mathcal{CN}(\mathbf{m}_1^\dagger, \sigma^2\mathbf{I}), \tag{24b}$$

where $\mathbf{m}_0^\dagger = \mathbf{Z}\mathbf{s}$ and $\mathbf{m}_1^\dagger = \mathbf{H}\mathbf{s} + \mathbf{Z}\mathbf{s}$. The GLRT detector decides $\mathcal{H}_1$ if [16]

$$\mathcal{L}(\mathbf{y}, \hat{\mathbf{H}}) = \frac{f(\mathbf{y}, \hat{\mathbf{H}};\mathcal{H}_1)}{f(\mathbf{y}, \hat{\mathbf{H}};\mathcal{H}_0)} > \varkappa, \tag{25}$$

where $\mathcal{L}(\mathbf{y}, \hat{\mathbf{H}})$ is the likelihood ratio, and $\hat{\mathbf{H}}$ is the maximum likelihood estimate (MLE) of $\mathbf{H}$, which can be computed as (Appendix B)

$$\hat{\mathbf{H}} = \mathbf{y}\mathbf{s}^H(\mathbf{s}\mathbf{s}^H)^{-1} - \mathbf{Z}. \tag{26}$$

In (25), $f(\mathbf{y}, \hat{\mathbf{H}};\mathcal{H}_0)$ and $f(\mathbf{y}, \hat{\mathbf{H}};\mathcal{H}_1)$ are the PDFs of $\mathbf{y}$ under $\mathcal{H}_0$ and $\mathcal{H}_1$, respectively. By using (24a) and (24b), the PDFs in (25) can be explicitly written as

$$f(\mathbf{y}, \hat{\mathbf{H}};\mathcal{H}_0) = \frac{e^{-(\mathbf{y}-\mathbf{m}_0^\dagger)^H \frac{1}{\sigma^2}\mathbf{I}^{-1}(\mathbf{y}-\mathbf{m}_0^\dagger)}}{\pi^{M_r}\det(\sigma^2\mathbf{I})}, \tag{27a}$$

$$f(\mathbf{y}, \hat{\mathbf{H}};\mathcal{H}_1) = \frac{e^{-(\mathbf{y}-\mathbf{m}_1^\dagger)^H \frac{1}{\sigma^2}\mathbf{I}^{-1}(\mathbf{y}-\mathbf{m}_1^\dagger)}}{\pi^{M_r}\det(\sigma^2\mathbf{I})}. \tag{27b}$$

Next, the likelihood ratio in (25) can be rewritten as

$$\mathcal{L}(\mathbf{y}, \hat{\mathbf{H}}) = \frac{e^{-(\mathbf{y}-\mathbf{m}_1^\dagger)^H \frac{1}{\sigma^2}\mathbf{I}^{-1}(\mathbf{y}-\mathbf{m}_1^\dagger)}}{e^{-(\mathbf{y}-\mathbf{m}_0^\dagger)^H \frac{1}{\sigma^2}\mathbf{I}^{-1}(\mathbf{y}-\mathbf{m}_0^\dagger)}} > \varkappa. \tag{28}$$

The log-likelihood ratio can be obtained by taking the logarithm of (28). Thus, the GLRT detector decides $\mathcal{H}_1$ if

$$\begin{aligned}\mathcal{T}(\mathbf{y}, \hat{\mathbf{H}}) &= \mathbf{y}^H(\mathbf{m}_1^\dagger - \mathbf{m}_0^\dagger) = \mathbf{y}^H\hat{\mathbf{H}}\mathbf{s} \\ &= \mathbf{y}^H\left(\mathbf{y}\mathbf{s}^H(\mathbf{s}\mathbf{s}^H)^{-1} - \mathbf{Z}\right)\mathbf{s} > \varkappa',\end{aligned} \tag{29}$$

where the modified threshold $\varkappa'$ is given by

$$\varkappa' = (1/2)\sigma^2\ln(\varkappa) + (1/2)\mathbf{s}^H\hat{\mathbf{H}}^H\hat{\mathbf{H}}\mathbf{s} + \mathbf{s}^H\mathbf{Z}^H\hat{\mathbf{H}}\mathbf{s}. \tag{30}$$

The PDFs of the test statistic $\mathcal{T}(\mathbf{y}, \hat{\mathbf{H}})$ under $\mathcal{H}_0$ and $\mathcal{H}_1$ can be written as

$$\mathcal{H}_0 : \mathcal{T}(\mathbf{y}, \hat{\mathbf{H}}) \sim \Gamma(\alpha_0, \beta_0), \tag{31a}$$

$$\mathcal{H}_1 : \mathcal{T}(\mathbf{y}, \hat{\mathbf{H}}) \sim \Gamma(\alpha_1, \beta_1), \tag{31b}$$

where $\alpha_0 = \bar{m}_0^2/\bar{v}_0$, $\beta_0 = \bar{m}_0/\bar{v}_0$, $\alpha_1 = \bar{m}_1^2/\bar{v}_1$ and $\beta_1 = \bar{m}_1/\bar{v}_1$. Here, $\bar{m}_0$ and $\bar{m}_1$ are derived as (Appendix C)

$$\bar{m}_0 = \sigma^2 M_r\mathbf{s}^H(\mathbf{s}\mathbf{s}^H)^{-1}\mathbf{s}, \tag{32}$$

$$\bar{m}_1 = \mathbf{s}^H\mathbf{H}^H\mathbf{H}\mathbf{s} + \mathbf{s}^H\mathbf{Z}^H\mathbf{H}\mathbf{s} + \sigma^2 M_r\mathbf{s}^H(\mathbf{s}\mathbf{s}^H)^{-1}\mathbf{s}. \tag{33}$$

Moreover, $\bar{v}_0$ and $\bar{v}_1$ can be derived as (34) and (35) at the top of the next page, respectively (Appendix C). Next, P_{FA} can be defined as

$$P_{FA} = \Pr\left(\mathcal{T}(\mathbf{y}, \hat{\mathbf{H}}) > \varkappa';\mathcal{H}_0\right), \tag{36}$$

$$\bar{v}_0 = \mathbf{s}^H\mathbf{Z}^H\mathbf{Z}\mathbf{s}\mathbf{s}^H((\mathbf{s}\mathbf{s}^H)^{-1})^H\mathbf{s}\mathbf{s}^H\mathbf{Z}^H\mathbf{Z}\mathbf{s} + \sigma^2 M_r\mathbf{s}^H\mathbf{Z}^H\mathbf{Z}\mathbf{s}\mathbf{s}^H((\mathbf{s}\mathbf{s}^H)^{-1})^H\mathbf{s} + \sigma^4(M_r^2+M_r)\mathbf{s}^H((\mathbf{s}\mathbf{s}^H)^{-1})^H\mathbf{s} - \mathbf{s}^H\mathbf{Z}^H\mathbf{Z}\mathbf{s}\mathbf{s}^H\mathbf{Z}^H\mathbf{Z}\mathbf{s}$$
$$-2\sigma^2 M_r\mathbf{s}^H\mathbf{Z}^H\mathbf{Z}\mathbf{s} + \sigma^2 M_r\mathrm{Tr}\Big(\mathbf{Z}\mathbf{s}\mathbf{s}^H\mathbf{Z}^H\Big) - (\sigma^2 M_r\mathbf{s}^H(\mathbf{s}\mathbf{s}^H)^{-1}\mathbf{s})^2. \quad (34)$$

$$\bar{v}_1 = (\mathbf{H}\mathbf{s}+\mathbf{Z}\mathbf{s})^H(\mathbf{H}\mathbf{s}+\mathbf{Z}\mathbf{s})\mathbf{s}^H((\mathbf{s}\mathbf{s}^H)^{-1})^H\mathbf{s}(\mathbf{H}\mathbf{s}+\mathbf{Z}\mathbf{s})^H(\mathbf{H}\mathbf{s}+\mathbf{Z}\mathbf{s}) + 2\sigma^2 M_r(\mathbf{H}\mathbf{s}+\mathbf{Z}\mathbf{s})^H(\mathbf{H}\mathbf{s}+\mathbf{Z}\mathbf{s})\mathbf{s}^H((\mathbf{s}\mathbf{s}^H)^{-1})^H\mathbf{s}$$
$$+\sigma^2\mathbf{s}^H((\mathbf{s}\mathbf{s}^H)^{-1})^H\mathbf{s}(\mathbf{H}\mathbf{s}+\mathbf{Z}\mathbf{s})^H(\mathbf{H}\mathbf{s}+\mathbf{Z}\mathbf{s}) + \sigma^2\mathbf{s}^H((\mathbf{s}\mathbf{s}^H)^{-1})^H\mathbf{s}\mathrm{Tr}\Big((\mathbf{H}\mathbf{s}+\mathbf{Z}\mathbf{s})(\mathbf{H}\mathbf{s}+\mathbf{Z}\mathbf{s})^H\Big) + \sigma^4(M_r^2+M_r)\mathbf{s}^H((\mathbf{s}\mathbf{s}^H)^{-1})^H\mathbf{s}$$
$$-2(\mathbf{H}\mathbf{s}+\mathbf{Z}\mathbf{s})^H(\mathbf{H}\mathbf{s}+\mathbf{Z}\mathbf{s})\mathbf{s}^H\mathbf{Z}(\mathbf{H}\mathbf{s}+\mathbf{Z}\mathbf{s}) - 2\sigma^2\mathrm{Tr}\Big((\mathbf{H}\mathbf{s}+\mathbf{Z}\mathbf{s})\mathbf{s}^H\mathbf{Z}^H\Big) - 2\sigma^2 M_r\mathbf{s}^H\mathbf{Z}^H(\mathbf{H}\mathbf{s}+\mathbf{Z}\mathbf{s})$$
$$+(\mathbf{H}\mathbf{s}+\mathbf{Z}\mathbf{s})^H\mathbf{Z}\mathbf{s}\mathbf{s}^H\mathbf{Z}^H(\mathbf{H}\mathbf{s}+\mathbf{Z}\mathbf{s}) + \sigma^2 M_r\mathrm{Tr}\Big(\mathbf{Z}\mathbf{s}\mathbf{s}^H\mathbf{Z}^H\Big) - (\mathbf{s}^H\mathbf{H}^H\mathbf{H}\mathbf{s} + \mathbf{s}^H\mathbf{Z}^H\mathbf{H}\mathbf{s} + \sigma^2 M_r\mathbf{s}^H(\mathbf{s}\mathbf{s}^H)^{-1}\mathbf{s})^2. \quad (35)$$

Algorithm 1 : Algorithm to solve power allocation coefficients optimization problem $\mathcal{P}_\rho$ in (40a)-(40e)

Input: $\tilde{\rho_s}$, P, K, $\mathbf{w}_{c,i}\forall i$, $\mathbf{w}_s$, σ_k
1: Compute $|\mathbf{f}_k\mathbf{w}_{c,k}|^2$, $|\mathbf{f}_k\mathbf{w}_s|^2$, and $|\mathbf{f}_k\mathbf{w}_{c,i}|^2 \ \ \forall i$.
2: Evaluate ${\rho_{c,k}}^* \ \forall k$ and ρ_s^* by solving $\mathcal{P}_\rho$ in (40a)-(40e).
Output: ${\rho_{c,k}}^* \ \forall k$, ρ_s^*

where $\varkappa'$ is given in (30). By using the CCDF of the Gamma distribution, P_{FA} can be derived as

$$P_{FA} = 1 - \frac{1}{\Gamma(\alpha_0)}\gamma(\alpha_0, \beta_0\varkappa'). \quad (37)$$

Then, P_D can be derived as

$$P_D = \Pr\Big(\mathcal{T}(\mathbf{y}, \hat{\mathbf{H}}) > \varkappa'; \mathcal{H}_1\Big) = 1 - \frac{1}{\Gamma(\alpha_1)}\gamma(\alpha_1, \beta_1\varkappa'). \quad (38)$$

IV. Transmit Power Optimization

In this section, an algorithm is developed to optimize the transmit power allocation coefficients for sensing and communications. The optimization problem is formulated based on the max-min fairness-based criterion to maximize the achievable DL rate of the weakest communication user, while satisfying a threshold ($\tilde{\rho_s}$) for sensing power allocation coefficient. We formulate the optimization problem for (6) as

$$\mathcal{P}_\rho: \max_{\rho_{c,k}\forall k,\rho_s} \ \min_k \ \gamma_k, \quad (39a)$$
$$\text{subject to } \mathrm{C}_1: \ \rho_{c,k}, \rho_s \geq 0 \ \ \forall k, \quad (39b)$$
$$\mathrm{C}_2: \ \sum\nolimits_{k=1}^{K}\rho_{c,k} + \rho_s \leq 1, \quad (39c)$$
$$\mathrm{C}_3: \ \rho_s \geq \tilde{\rho_s}. \quad (39d)$$

By defining a lower bound $\bar{\gamma}$ to the SINR at all K users, the max-min optimization problem in (39a)-(39d) can be equivalently reformulated as

$$\mathcal{P}_\rho: \max_{\rho_{c,k}\forall k,\rho_s} \ \bar{\gamma}, \quad (40a)$$
$$\text{subject to } \mathrm{C}_1: \ \rho_{c,k}, \rho_s \geq 0 \ \ \forall k, \quad (40b)$$
$$\mathrm{C}_2: \ \sum\nolimits_{k=1}^{K}\rho_{c,k} + \rho_s \leq 1, \quad (40c)$$
$$\mathrm{C}_3: \ \rho_s \geq \tilde{\rho_s}, \quad (40d)$$
$$\mathrm{C}_4: \rho_{c,k}P|\mathbf{f}_k\mathbf{w}_{c,k}|^2 \geq \rho_s P\bar{\gamma}|\mathbf{f}_k\mathbf{w}_s|^2 + P\bar{\gamma}\sum\nolimits_{i\neq k}^{K}\rho_{c,i}|\mathbf{f}_k\mathbf{w}_{c,i}|^2 + \sigma_k^2\bar{\gamma}. \quad (40e)$$

The above optimization problem (40a)-(40e) can be solved via geometric programming (GP) using a convex solver. Our optimization procedure can be summarized as Algorithm-1.

V. The trade-off between P_D and $\mathcal{R}_k$

The achievable rate ($\mathcal{R}_k$) in (7), and P_D in (23) and (38) can be used to quantify the ISAC performance trade-offs. By varying the transmit power allocation coefficient for sensing as $\rho_s \in [0,1]$, the trade-off between $\mathcal{R}_k$ and P_D can be studied. The remainder of the available transmit power can be allocated to the users based on the max-min criterion as

$$\mathcal{P}'_\rho: \max_{\rho_{c,k}\forall k,\rho_s} \ \bar{\gamma}, \quad (41a)$$
$$\text{subject to } \mathrm{C}_1: \ \rho_{c,k}, \rho_s \geq 0 \ \ \forall k, \quad (41b)$$
$$\mathrm{C}_2: \ \sum\nolimits_{k=1}^{K}\rho_{c,k} + \rho_s \leq 1, \quad (41c)$$
$$\mathrm{C}_3: \rho_{c,k}P|\mathbf{f}_k\mathbf{w}_{c,k}|^2 \geq \rho_s P\bar{\gamma}|\mathbf{f}_k\mathbf{w}_s|^2 + P\bar{\gamma}\sum\nolimits_{i\neq k}^{K}\rho_{c,i}|\mathbf{f}_k\mathbf{w}_{c,i}|^2 + \sigma_k^2\bar{\gamma}, \quad (41d)$$

which can also be solved via GP with a convex solver. Thus, by adopting (7), (23), (38), and (41a)-(41d), the trade-off between $\mathcal{R}_k$ and P_D can be quantified by traversing through the common points of $\rho_s \in [0,1]$.

VI. Numerical Results

We set the carrier frequency to $f_0 = 28$ GHz such that $\lambda = 10.71$ mm. We consider an ISAC system equipped with an ELAA with $M_t = 400$ and $M_r = 200$. We set $L_h = 0.16$ m, $L_v = 0.46$ m, $A = (\lambda/4)^2$, $d_h = 0.5\lambda$, and $d_v = 2\lambda$. The noise variance is modeled as $\sigma_n^2 = 10\log_{10}(N_0 B N_F)$, where $N_0 = -174$ dBm/Hz, $B = 100$ MHz, and $N_F = 7$ dB. The system consists of $K = 5$ communication users and a single target. The BS-users and BS-target distances are set to $[20, 30, 35, 40, 10]$ m and 20 m, respectively, such that the distances fall below Fraunhofer distance ($d_F = 44.13$ m) to guarantee that the users and target are located in the near-field. Monte-Carlo simulations are used to validate our numerical results in the context of an ISAC scenario that has been examined for two different cases, namely (i) Case-1: known sensing channel, and (ii) Case-2: unknown sensing channel.

In Fig. 2, the trade-off between the P_D and achievable DL user rate for ISAC is studied. Two scenarios, namely Case-1: known sensing channel ($\mathbf{H}$) and Case-2: unknown sensing channel ($\hat{\mathbf{H}}$) are considered for three different P_{FA} values such that $P_{FA} \in \{0.1, 0.01, 0.001\}$. The trade-off curves are plotted by varying the transmit power allocation coefficients for the sensing signal (ρ_s) from 0 to 1. A system-wide common user rate for each sensing power allocation coefficient point has been achieved through our optimization problem (41a)-(41d). For instance, at $\rho_s = 0.2$, in the system with $P_{FA} = 0.1$, an achievable rate of 0.996 bits/s/Hz can

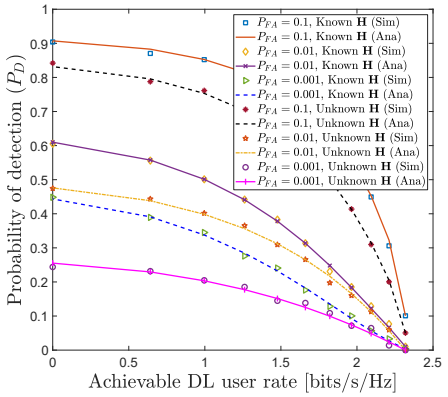

Fig. 2. The trade-off between probability of detection and achievable DL user rate for $K=5$, $M_t=400$ and $M_r=200$.

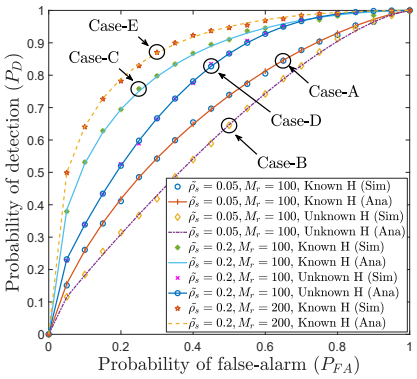

Fig. 3. The ROC: Probability of detection versus probability of false-alarm for $K=5$ and $M_t=400$.

be obtained while achieving a P_D of 0.853 and 0.761 for the Case-1 and Case-2, respectively. Fig. 2 provides a useful insight that availability of sensing channel knowledge at the BS can increase its detection probability. For instance, at $\rho_s=0.2$, the system with target sensing channel knowledge outperforms the system without BS-target channel knowledge by 13.28%, 24.63% and 69.95%, for $P_{FA}=0.1$, $P_{FA}=0.01$ and $P_{FA}=0.001$, respectively. This observation unveils that in the lower P_{FA} regime, the detection probability drastically reduces in the absence of BS-target channel knowledge. Hence, Fig. 2 unveils that achievable rates can be increased at the expense of P_D thus constituting a fundamental ISAC performance trade-off. Fig. 2 also reveals that this trade-off can be improved by adopting ELAAs for ISAC.

Fig. 3 presents the ROC curves depicting the fundamental trade-off between P_D and P_{FA} for both the cases of known and unknown sensing channels. The Case-A, -C and -E correspond to the scenario of known sensing channel. The Case-B and Case-D correspond to the scenario of unknown sensing channel. For Case-A, -B, -C and -D, $M_r=100$ has been used, whereas Case-E has been plotted for $M_r=200$. For instance, at $P_{FA}=0.4$, P_D decreases by 16.42% and 9.56% in Case-B compared to Case-A and Case-D compared to Case-C, respectively. This implies that the unavailability of sensing channel knowledge at the BS decreases the detection capability of the detector. Fig. 3 reveals that the detection capability increases with the increased threshold for target

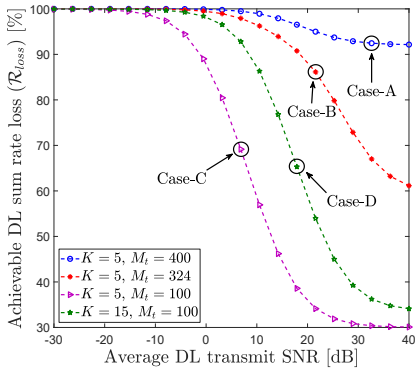

Fig. 4. Percentage rate loss: $M_t\in\{100,324,400\}$, $M_r=200$, $\tilde{\rho}_s=0.01$ and $K\in\{5,15\}$.

sensing power allocation coefficient ($\tilde{\rho}_s$). The impact of number of receive antennas (M_r) is also studied through ROC curves for known sensing channel under two cases, namely Case-C ($M_r=100$) and Case-E ($M_r=200$). We observe that by the detection probability can be boosted by increasing M_r. For instance, at $P_{FA}=0.4$, P_D can be increased by 6.39% when number of receive antennas increases from $M_r=100$ to $M_r=200$.

The Fig. 4 depicts the percentage sum rate losses incurred due to near/far-field channel mismatches for $M_t\in\{100,324,400\}$, $M_r=200$, $\tilde{\rho}_s=0.01$ and $K\in\{5,15\}$. The percentage sum rate loss is quantified by using $\mathcal{R}_{loss}=(\mathcal{R}'-\mathcal{R}^{\ddagger})/\mathcal{R}'\times 100\,\%$, where $\mathcal{R}'$ and $\mathcal{R}^{\ddagger}$ are the sum rates offered by systems with near-field and far-field assumptions, respectively. The Case-A, -B and -C correspond to the set-ups with $M_t=400$, $M_t=324$ and $M_t=100$, respectively for $K=5$. The Case-D corresponds to the set-up with $M_t=100$ and $K=15$. We utilize Algorithm-1 for optimized power allocation to guarantee system-wide user-fairness. At transmit signal-to-noise ratio (SNR) of 30 dB, a system with $K=5$ near-field users loss the sum rate by 92.89%, 72.87%, and 30.84% for $M_t=400$, $M_t=324$ and $M_t=100$, respectively, due to the use of precoders designed with far-field assumption while the users are located in the near-field. This result unveils that the higher number of transmit antennas could worsen the impact of inaccurate assumption of far-field for the near-field communication users. We also observe that the rate loss increases with K. For instance, the rate loss for Case-C with $K=5$ and Case-D with $K=15$ are 30.84% and 39.27%, respectively, at transmit SNR 30 dB. We conclude that significant rate losses can incur when far-field precoders are used for the users located in near-field in ISAC systems.

VII. Conclusion

The trade-off between the probability of detection and achievable user rates of ELAA-based near-field ISAC systems has been investigated. The precoders for the sensing and communication signals have been constructed based on the MRT principle to ensure simple implementation. The achievable rate, probability of detection/false-alarm, and ROC have been used to investigate the performance of ELAA-based near-field ISAC. A transmit power allocation algorithm has also been proposed to maximize the minimum achievable user rate,

while ensuring a minimum sensing power threshold. Based on our analysis and numerical results, it is advocated to use near-field precoders when the users/target are located in the near-field to enhance rate/detection probability and to avoid mismatches between near/far-field channel models.

APPENDIX A
DERIVATION OF $\tilde{m}_0$, $\tilde{m}_1$, $\tilde{v}_0$ AND $\tilde{v}_1$ IN (18)-(19)

The means $\tilde{m}_0$ and $\tilde{m}_1$ of the test statistic $\mathcal{T}(\mathbf{y})$ under $\mathcal{H}_0$ and $\mathcal{H}_1$ can be derived as

$$\begin{aligned}\mathbb{E}[\mathcal{T}(\mathbf{y});\mathcal{H}_0] &= \tilde{m}_0 = \mathbb{E}\Big[\mathbf{y}^H\mathbf{H}\mathbf{s};\mathcal{H}_0\Big]\\ &= \mathbb{E}\Big[(\mathbf{Z}\mathbf{s}+\mathbf{n})^H\mathbf{H}\mathbf{s}\Big] = \mathbf{s}^H\mathbf{Z}^H\mathbf{H}\mathbf{s}, \quad (42)\\ \mathbb{E}[\mathcal{T}(\mathbf{y});\mathcal{H}_1] &= \tilde{m}_1 = \mathbb{E}\Big[\mathbf{y}^H\mathbf{H}\mathbf{s};\mathcal{H}_1\Big]\\ &= \mathbb{E}\Big[(\mathbf{H}\mathbf{s}+\mathbf{Z}\mathbf{s}+\mathbf{n})^H\mathbf{H}\mathbf{s}\Big] = \mathbf{s}^H\mathbf{H}^H\mathbf{H}\mathbf{s}+\mathbf{s}^H\mathbf{Z}^H\mathbf{H}\mathbf{s}, \quad (43)\end{aligned}$$

where $\mathbf{n}\sim\mathcal{CN}(\mathbf{0},\sigma^2\mathbf{I})$. Next, the variances $\tilde{v}_0$ and $\tilde{v}_1$ of the test statistic $\mathcal{T}(\mathbf{y})$ under $\mathcal{H}_0$ and $\mathcal{H}_1$ can be derived as

$$\begin{aligned}\tilde{v}_0 &= \mathbb{E}\left[\left(\mathbf{y}^H\mathbf{H}\mathbf{s}-\mathbb{E}\Big[\mathbf{y}^H\mathbf{H}\mathbf{s}\Big]\right)^2;\mathcal{H}_0\right]\\ &= \mathbb{E}\left[\left((\mathbf{Z}\mathbf{s}+\mathbf{n})^H\mathbf{H}\mathbf{s}-\mathbf{s}^H\mathbf{Z}^H\mathbf{H}\mathbf{s}\right)^2\right]\\ &= \mathbb{E}\left[\left(\mathbf{s}^H\mathbf{Z}^H\mathbf{H}\mathbf{s}+\mathbf{n}^H\mathbf{H}\mathbf{s}-\mathbf{s}^H\mathbf{Z}^H\mathbf{H}\mathbf{s}\right)^2\right] = \sigma^2\mathbf{s}^H\mathbf{H}^H\mathbf{H}\mathbf{s}, \quad (44)\\ \tilde{v}_1 &= \mathbb{E}\left[\left(\mathbf{y}^H\mathbf{H}\mathbf{s}-\mathbb{E}\Big[\mathbf{y}^H\mathbf{H}\mathbf{s}\Big]\right)^2;\mathcal{H}_1\right]\\ &= \mathbb{E}\left[\left((\mathbf{H}\mathbf{s}+\mathbf{Z}\mathbf{s}+\mathbf{n})^H\mathbf{H}\mathbf{s}-\left(\mathbf{s}^H\mathbf{H}^H\mathbf{H}\mathbf{s}+\mathbf{s}^H\mathbf{Z}^H\mathbf{H}\mathbf{s}\right)\right)^2\right]\\ &= \sigma^2\mathbf{s}^H\mathbf{H}^H\mathbf{H}\mathbf{s}. \quad (45)\end{aligned}$$

APPENDIX B
DERIVATION OF $\hat{\mathbf{H}}$ IN (26)

The MLE of $\mathbf{H}$ can be derived by using (27b) as

$$\begin{aligned}&\frac{\partial\ln(f(\mathbf{y},\hat{\mathbf{H}};\mathcal{H}_1))}{\partial\mathbf{H}} = \mathbf{0}\\ &\frac{\partial}{\partial\mathbf{H}}\left[-(\mathbf{y}-\mathbf{m}_1^\dagger)^H\frac{1}{\sigma^2}\mathbf{I}^{-1}(\mathbf{y}-\mathbf{m}_1^\dagger)-\ln\left(\pi^{M_r}\det(\sigma^2\mathbf{I})\right)\right]=\mathbf{0}\\ &\frac{\partial}{\partial\mathbf{H}}\left[-(\mathbf{y}-\mathbf{H}\mathbf{s}-\mathbf{Z}\mathbf{s})^H\frac{1}{\sigma^2}\mathbf{I}^{-1}(\mathbf{y}-\mathbf{H}\mathbf{s}-\mathbf{Z}\mathbf{s})\right]=\mathbf{0}\\ &\hat{\mathbf{H}} = \mathbf{y}\mathbf{s}^H(\mathbf{s}\mathbf{s}^H)^{-1}-\mathbf{Z}. \quad (46)\end{aligned}$$

APPENDIX C
DERIVATION OF $\bar{m}_0$, $\bar{m}_1$, $\bar{v}_0$ AND $\bar{v}_1$ IN (32)-(35)

The means $\bar{m}_0$ and $\bar{m}_1$ of the test statistic $\mathcal{T}(\mathbf{y},\hat{\mathbf{H}})$ under $\mathcal{H}_0$ and $\mathcal{H}_1$ can be derived as

$$\begin{aligned}&\mathbb{E}\Big[\mathcal{T}(\mathbf{y},\hat{\mathbf{H}});\mathcal{H}_0\Big] = \bar{m}_0 = \mathbb{E}\Big[\mathbf{y}^H\left(\mathbf{y}\mathbf{s}^H(\mathbf{s}\mathbf{s}^H)^{-1}-\mathbf{Z}\right)\mathbf{s};\mathcal{H}_0\Big]\\ &= \mathbb{E}\Big[(\mathbf{Z}\mathbf{s}+\mathbf{n})^H(\mathbf{Z}\mathbf{s}+\mathbf{n})\mathbf{s}^H(\mathbf{s}\mathbf{s}^H)^{-1}\mathbf{s}-(\mathbf{Z}\mathbf{s}+\mathbf{n})^H\mathbf{Z}\mathbf{s}\Big]\\ &= \sigma^2M_r\mathbf{s}^H(\mathbf{s}\mathbf{s}^H)^{-1}\mathbf{s}, \quad (47)\\ &\mathbb{E}\Big[\mathcal{T}(\mathbf{y},\hat{\mathbf{H}});\mathcal{H}_1\Big] = \bar{m}_1 = \mathbb{E}\Big[\mathbf{y}^H\left(\mathbf{y}\mathbf{s}^H(\mathbf{s}\mathbf{s}^H)^{-1}-\mathbf{Z}\right)\mathbf{s};\mathcal{H}_1\Big]\\ &= \mathbb{E}\Big[(\mathbf{H}\mathbf{s}+\mathbf{Z}\mathbf{s}+\mathbf{n})^H(\mathbf{H}\mathbf{s}+\mathbf{Z}\mathbf{s}+\mathbf{n})\mathbf{s}^H(\mathbf{s}\mathbf{s}^H)^{-1}\mathbf{s}\\ &\quad-(\mathbf{H}\mathbf{s}+\mathbf{Z}\mathbf{s}+\mathbf{n})^H\mathbf{Z}\mathbf{s}\Big]\\ &= \mathbf{s}^H\mathbf{H}^H\mathbf{H}\mathbf{s}+\mathbf{s}^H\mathbf{Z}^H\mathbf{H}\mathbf{s}+\sigma^2M_r\mathbf{s}^H(\mathbf{s}\mathbf{s}^H)^{-1}\mathbf{s}, \quad (48)\end{aligned}$$

where $\mathbf{n}\sim\mathcal{CN}(\mathbf{0},\sigma^2\mathbf{I})$. Next, the variances $\bar{v}_0$ and $\bar{v}_1$ of the test statistic $\mathcal{T}(\mathbf{y},\hat{\mathbf{H}})$ under $\mathcal{H}_0$ and $\mathcal{H}_1$ can be derived as

$$\begin{aligned}\bar{v}_0 &= \mathbb{E}\left[\left(\mathbf{y}^H\left(\mathbf{y}\mathbf{s}^H(\mathbf{s}\mathbf{s}^H)^{-1}-\mathbf{Z}\right)\mathbf{s}-\bar{m}_0\right)^2;\mathcal{H}_0\right]\\ &= \mathbb{E}\Big[(\mathbf{Z}\mathbf{s}+\mathbf{n})^H(\mathbf{Z}\mathbf{s}+\mathbf{n})\mathbf{s}^H(\mathbf{s}\mathbf{s}^H)^{-1}\mathbf{s}(\mathbf{Z}\mathbf{s}+\mathbf{n})^H(\mathbf{Z}\mathbf{s}+\mathbf{n})\\ &\quad-(\mathbf{Z}\mathbf{s}+\mathbf{n})^H(\mathbf{Z}\mathbf{s}+\mathbf{n})\mathbf{s}^H\mathbf{Z}^H(\mathbf{Z}\mathbf{s}+\mathbf{n})\\ &\quad-(\mathbf{Z}\mathbf{s}+\mathbf{n})^H\mathbf{Z}\mathbf{s}(\mathbf{Z}\mathbf{s}+\mathbf{n})^H(\mathbf{Z}\mathbf{s}+\mathbf{n})\\ &\quad+(\mathbf{Z}\mathbf{s}+\mathbf{n})^H\mathbf{Z}\mathbf{s}\mathbf{s}^H\mathbf{Z}^H(\mathbf{Z}\mathbf{s}+\mathbf{n})\Big]-\bar{m}_0^2, \quad (49)\\ \bar{v}_1 &= \mathbb{E}\left[\left(\mathbf{y}^H\left(\mathbf{y}\mathbf{s}^H(\mathbf{s}\mathbf{s}^H)^{-1}-\mathbf{Z}\right)\mathbf{s}-\bar{m}_1\right)^2;\mathcal{H}_1\right]\\ &= \mathbb{E}\Big[(\mathbf{H}\mathbf{s}+\mathbf{Z}\mathbf{s}+\mathbf{n})^H(\mathbf{H}\mathbf{s}+\mathbf{Z}\mathbf{s}+\mathbf{n})\mathbf{s}^H(\mathbf{s}\mathbf{s}^H)^{-1}\mathbf{s}\\ &\quad\times(\mathbf{H}\mathbf{s}+\mathbf{Z}\mathbf{s}+\mathbf{n})^H(\mathbf{H}\mathbf{s}+\mathbf{Z}\mathbf{s}+\mathbf{n})-(\mathbf{H}\mathbf{s}+\mathbf{Z}\mathbf{s}+\mathbf{n})^H\\ &\quad\times(\mathbf{H}\mathbf{s}+\mathbf{Z}\mathbf{s}+\mathbf{n})\mathbf{s}^H\mathbf{Z}^H(\mathbf{H}\mathbf{s}+\mathbf{Z}\mathbf{s}+\mathbf{n})-(\mathbf{H}\mathbf{s}+\mathbf{Z}\mathbf{s}+\mathbf{n})^H\\ &\quad\times\mathbf{Z}\mathbf{s}(\mathbf{H}\mathbf{s}+\mathbf{Z}\mathbf{s}+\mathbf{n})^H(\mathbf{H}\mathbf{s}+\mathbf{Z}\mathbf{s}+\mathbf{n})+(\mathbf{H}\mathbf{s}+\mathbf{Z}\mathbf{s}+\mathbf{n})^H\\ &\quad\times\mathbf{Z}\mathbf{s}\mathbf{s}^H\mathbf{Z}^H(\mathbf{H}\mathbf{s}+\mathbf{Z}\mathbf{s}+\mathbf{n})\Big]-\bar{m}_1^2, \quad (50)\end{aligned}$$

where the final expressions for $\bar{v}_0$ and $\bar{v}_1$ have been given in (34) and (35), respectively.

REFERENCES

[1] J. A. Zhang *et al.*, "An Overview of Signal Processing Techniques for Joint Communication and Radar Sensing," *IEEE J. Sel. Topics Signal Process.*, vol. 15, no. 6, pp. 1295–1315, Nov. 2021.

[2] F. Liu *et al.*, "Integrated Sensing and Communications: Toward Dual-Functional Wireless Networks for 6G and Beyond," *IEEE J. Sel. Areas Commun.*, vol. 40, no. 6, pp. 1728–1767, Jun. 2022.

[3] Z. Wei *et al.*, "Integrated Sensing and Communication Signals Toward 5G-A and 6G: A Survey," *IEEE Internet Things J.*, vol. 10, no. 13, pp. 11 068–11 092, Jul. 2023.

[4] A. Liu *et al.*, "A Survey on Fundamental Limits of Integrated Sensing and Communication," *IEEE Commun. Surveys Tuts.*, vol. 24, no. 2, pp. 994–1034, Feb. 2022.

[5] N. Zhao *et al.*, "Joint Transmit and Receive Beamforming Design for Integrated Sensing and Communication," *IEEE Commun. Lett.*, vol. 26, no. 3, pp. 662–666, Mar. 2022.

[6] Z. Wang *et al.*, "NOMA Empowered Integrated Sensing and Communication," *IEEE Commun. Lett.*, vol. 26, no. 3, pp. 677–681, Mar. 2022.

[7] Z. Xiao and Y. Zeng, "Waveform Design and Performance Analysis for Full-Duplex Integrated Sensing and Communication," *IEEE J. Sel. Areas Commun.*, vol. 40, no. 6, pp. 1823–1837, Jun. 2022.

[8] J. An, H. Li, D. W. K. Ng, and C. Yuen, "Fundamental Detection Probability vs. Achievable Rate Tradeoff in Integrated Sensing and Communication Systems," *IEEE Trans. Wireless Commun.*, vol. 22, no. 12, pp. 9835–9853, Dec. 2023.

[9] Z. He *et al.*, "Energy Efficient Beamforming Optimization for Integrated Sensing and Communication," *IEEE Wireless Commun. Lett.*, vol. 11, no. 7, pp. 1374–1378, Jul. 2022.

[10] P. Ramezani and E. Björnson, "Near-Field Beamforming and Multiplexing using Extremely Large Aperture Arrays," *arXiv:2209.03082*, 2022.

[11] G. Bacci, L. Sanguinetti, and E. Björnson, "Spherical Wavefronts Improve MU-MIMO Spectral Efficiency When Using Electrically Large Arrays," Jul. 2023.

[12] E. Björnson, Ö. T. Demir, and L. Sanguinetti, "A Primer on Near-Field Beamforming for Arrays and Reconfigurable Intelligent Surfaces," in *2021 55th Asilomar Conference on Signals, Systems, and Computers*, 2021, pp. 105–112.

[13] C. B. Barneto *et al.*, "Full Duplex Radio/Radar Technology: The Enabler for Advanced Joint Communication and Sensing," *IEEE Wireless Commun. Mag.*, vol. 28, no. 1, pp. 82–88, Feb. 2021.

[14] M. Temiz, E. Alsusa, and M. W. Baidas, "A Dual-Function Massive MIMO Uplink OFDM Communication and Radar Architecture," *IEEE Trans. on Cogn. Commun. Netw.*, vol. 8, no. 2, pp. 750–762, Jun. 2022.

[15] Z. He *et al.*, "Full-Duplex Communication for ISAC: Joint Beamforming and Power Optimization," *IEEE J. Sel. Areas Commun.*, Sep. 2023.

[16] S. M. Kay, *Fundamentals of Statistical Signal Processing: Detection Theory*. Upper Saddle River, NJ, USA: Prentice-Hall, Inc., 1993.